

M2 INTERNSHIP REPORT

Modelling the Interior Composition of Sub-Neptune Exoplanets: The case of K2-18 b planet

Pauline Lomba M2 ASEP

Supervisor: João Medonça

Laboratory: DTU Space, Technical University of Denmark

Duration: 29/01/2024 – 28/06/2024

August 9, 2024

“Don’t panic!”

— *Douglas Adams, The Hitchhiker’s Guide to the Galaxy*

Abbreviations

M_p	Planet total mass
R_p	Planet total radius
M_{\oplus}	Earth total mass ($= 5.972 \cdot 10^{24}$ kg)
M_{\odot}	Sun total mass ($= 2 \cdot 10^{30}$ kg)
R_{\odot}	Sun total radius ($= 696340$ km)
L_{\odot}	Sun total luminosity ($= 3.846 \cdot 10^{26}$ watts)
AU	Astronomical unit ($= 1.495978707 \cdot 10^{11}$ m)
T_{eq}	Equilibrium temperature
P-T	Pressure-Temperature
G	Gravitational constant ($= 6.674 \cdot 10^{-11}$ N.m 2 .kg $^{-2}$)

Acknowledgements

I want to express my sincere gratitude to João Medonça, my internship supervisor, for helping me navigate through this process. He wisely and patiently answered all my questions and always showed kindness and understanding, making me feel supported at every step of this project.

I also want to extend my thanks to all the members of the Exoplanets research group at DTU Space for their guidance and generosity. I am grateful for the opportunity they provided me to be a part of their team and to see what the job of research is like.

Working with such a talented and supportive group of people has been a truly enriching experience, and I am thankful for the knowledge and skills I have gained during this internship.

Abstract

French

L'exploration des exoplanètes et l'analyse de leurs masses et de leurs rayons nous ont révélé une large gamme de densités moyennes, fournissant des informations précieuses sur leur structure interne. Malgré ces avancées, la différenciation - séparation en couches de compositions distinctes - de ces astres introduit des dégénérescences parmi leurs compositions potentielles, ce qui complique la détermination de leurs propriétés internes.

Nous présentons ici une nouvelle approche pour relever ce défi en combinant un modèle de structure interne de planète en 1D, MAGRATHEA, avec un algorithme d'échantillonnage imbriqué, UltraNest. Notre objectif est de contraindre la structure interne des exoplanètes les plus répandues dans notre galaxie, à savoir les planètes plus grandes que la Terre mais plus petites que Neptune (entre 1 et 4 R \oplus)[1]. Pour la modélisation de ces intérieurs, nous considérons quatre couches possibles: un noyau de fer, un manteau composé de silicates, une hydroosphère composée d'eau/de glace, et une atmosphère composée d'un mélange d'hydrogène/hélium. En utilisant des techniques d'échantillonnage imbriqué, nous visons à explorer les compositions possibles et à discriminer la ou les plus probables. Enfin, nous utilisons notre modèle pour étudier K2-18b, actuellement l'une des exoplanètes les plus prometteuses en termes d'habitabilité et qui suscite de vifs débats sur sa structure interne.

Nous comparons nos recherches avec des études précédentes pour valider l'efficacité de notre approche, et les résultats de ce projet contribueront à améliorer la compréhension des intérieurs exoplanétaires, essentielle dans l'étude de leur climat et de leurs conditions d'habitabilité.

English

The exploration of exoplanets has revealed a wide range of planetary bulk compositions through the analysis of their masses and radii, leading to valuable insights into their internal structure. However, the differentiation of exoplanets' interiors into distinct layers introduces degeneracies among possible compositions, complicating efforts to accurately infer their internal properties.

Here, we present a novel approach to address this challenge by combining a 1D planet interior structure model, MAGRATHEA, with a nested sampling algorithm, UltraNest. Our goal is to constrain the interior structure of the most populous class of planets in our galaxy, which are planets larger than Earth but smaller than Neptune (between 1-4 R \oplus)[1]. For the planet's interior, we consider four possible components: an iron core, a mantle of silicates, an hydrosphere composed of water/ice covered by an H₂-dominated atmosphere in ideal gas conditions. By employing nested sampling techniques, we aim to explore the parameter space and discriminate between various compositional models. We finally use our work to study K2-18b, one of the most promising exoplanets for habitability that creates debate on its real composition.

We compare our results with previous studies to validate the effectiveness of our approach. The results of our project will help enhance our understanding of exoplanetary interiors, which are crucial in driving planets' climates and creating habitable conditions.

Contents

1	Introduction	1
1.1	M dwarf opportunity	1
1.2	Detection methods	2
1.3	Exoplanets classification	3
1.3.1	Super-Earths and sub-Neptune planets	4
1.3.2	Hycean worlds	4
1.4	Our study case: K2-18b	5
2	Internal composition constraints	6
2.1	Formation	6
2.2	Host star	6
2.3	Structure	7
2.4	Atmosphere	8
3	Models used	9
3.1	MAGRATHEA	9
3.1.1	Model equations[2]	10
3.1.2	Phase diagrams[2]	11
3.1.3	Chemistry[2]	11
3.2	UltraNest	13
4	Our model	13
4.1	Environment	13
4.2	Inputs	14
4.3	UltraNest algorithm	14
4.3.1	Prior fonction	14
4.3.2	Log-likelihood	15
4.3.3	Global parameters	16
4.4	Outputs	17
4.5	Benchmark tests	17
4.5.1	Two-layer planet	17
4.5.2	Three-layer planet	18
4.5.3	Four-layer planet	20
4.6	Other parameters	20
5	K2-18b case	20
5.0.1	Main composition	20
5.0.2	Atmosphere	22
5.0.3	Core	23
5.1	Comparative analysis	24
6	Discussion	25
7	Perspectives	26
8	Limitations	27
9	Conclusion	28

1 Introduction

Our objective is to unravel the composition and structure of a specific class of exoplanets: the sub-Neptunes. To achieve this, let us start by discussing the types of stars around which we observe exoplanets, the methods used in planet detection, followed by a closer examination of the category of planets relevant to our study, sub-Neptunes, and at last we will focus on the exoplanet K2-18b.

1.1 M dwarf opportunity

Stars are classified by letters from the hottest to the coolest; we have: OBAFGKM. The coolest and most promising are the M-type stars, also called M dwarfs¹.

M dwarf presents a real advantage when it comes to exoplanets detection, first, they stand out as the most abundant stellar type in our galaxy, 70%[3] and 80% of our close solar neighborhood[4][5]. They also possess a minimum of twice the number of small exoplanets with $M_p \sin i < 10M_{\oplus}$ compared to G-type stars [6], i being the inclination angle of the orbital plane relative to the line of sight from Earth.

Due to their small size ($0.1\text{--}0.6 R_{\odot}$)² and masses ($0.08\text{--}0.6 M_{\odot}$)², planets orbiting M dwarfs are easier to detect compared to planets of the same size orbiting a larger star. The two main stellar parameters for the detection of exoplanets are mass and size. The size is particularly significant because the depth of the eclipse during the planet's transit depends on the ratio of the planet's radius to the star's radius. Additionally, as the mass of the star increases, the amplitude of the radial velocity decreases. This is why planets orbiting M dwarfs, despite their smaller size and mass, have a relatively larger effect on their host stars, making them wobble more (see section 1.2)[7]. In contrast, but logically, the easiest planets to detect are the large and hot exoplanets. Having low mass also means M dwarfs are very long-lived, stellar models suggest they could exist for trillions of years, which is far more than the current age of the universe, the lower the mass of a red dwarf, the longer the lifespan[8].

However their low luminosity ($0.069\text{--}3.0 \cdot 10^{-4} L_{\odot}$)² and indeed their magnitude can complicate the detection, especially when the planet is very small. This is because the faintness of the star makes it more difficult to distinguish the tiny dip in brightness caused by the small planet passing in front of it. Additionally, this low luminosity may result in a lower signal-to-noise ratio, further complicating the detection process.

Moreover, the cooler temperatures of M dwarfs compared to solar-type stars result in planets located within their habitable zones - regions where conditions could support liquid water on the surface - being situated nearer to their host star. This proximity corresponds to orbital periods that are typically well covered by current surveys, such as approximately 60 days for a big M0 star and 3 days for a small M9 star, thus aiding in their detection and characterization[7]. But on the other hand, this close proximity raises concerns about tidal locking - when the same side of the planet always faces the star - and stellar irradiation effects, which could influence their habitability[9]

¹Source: <https://media4.obspm.fr/public/ressources/u/pages,observation/bb-type-spectral.html>

²Source: https://en.wikipedia.org/wiki/Red_dwarf

Finally, the only main problem about M dwarfs is their stellar flares, which exhibit more than solar-type stars due to their more intense magnetic activity, which arises from their rapid rotation and low mass[10]. This greater stellar activity can introduce noise into observational data, complicating the differentiation between planetary signals and stellar variability[11], and again potentially impacting the habitability of nearby planets[12].

Nevertheless, this opportunity for research and study of exoplanets through M dwarfs called the "M dwarf opportunity," has resulted in numerous detection of highly encouraging low-mass planets ($< 10M_{\oplus}$) within the habitable zones of M-dwarf hosts, including TRAPPIST-1[13], Proxima Centauri[14], and K2-18[15].

1.2 Detection methods

Various methods have been used to detect exoplanets, allowing us to deduce the main planet parameters. The main goal of this project is to study the internal composition of exoplanets based on observationally determined mass and radius, thus deriving the bulk density. Additionally, we'll analyze its spectra to study its atmosphere (see section 2.4). The transit method is best for radius characterization, while radial velocity is optimal for mass determination.

Transiting planets are those that pass in front of their parent star, causing the starlight to dim by an amount equal to the planet-to-star area ratio. Assuming the stellar disc is uniformly bright and neglecting any flux from the planet, we can simplify the calculation by disregarding the limb-darkening effect. With knowledge of the star's size, we can then infer the size of the exoplanet using the following formula:

$$\frac{\Delta f}{f} = \left(\frac{R_p}{R_{\text{star}}} \right)^2 \quad (1)$$

Where $\frac{\Delta f}{f}$ represents the fractional flux deficit measured from the light curve³.

The radial velocity method, also known as the Doppler spectroscopy measures the variations in the radial velocity of the star induced by the gravitational influence of its orbiting planets (see Figure 1). We can have access to the planet's mass by combining Kepler's Third Law and this equation[16]:

$$v_r = K \sin(i) \quad (2)$$

Where v_r is the radial velocity, K is the amplitude of the radial velocity curve (related to the mass of the planet and the orbital parameters) and i as previously said is the inclination angle of the orbital plane relative to the line of sight from Earth. However, it's important to note that in many cases, only a lower limit on the planet's mass can be determined using the radial velocity method, because the inclination angle of the orbit may not be known⁴. If the orbit is observed nearly edge-on ($i \approx 90^\circ$), then the measured radial velocity provides a good estimate of the planet's true mass. Otherwise, the measured radial velocity gives only a minimum mass (referred to as the "minimum mass" or " $M \sin(i)$ ")⁴.

³Source: <https://www.paulanthonywilson.com/exoplanets/exoplanet-detection-techniques/the-exoplanet-transit-method/>

⁴Source: <https://www.planetary.org/articles/color-shifting-stars-the-radial-velocity-method>

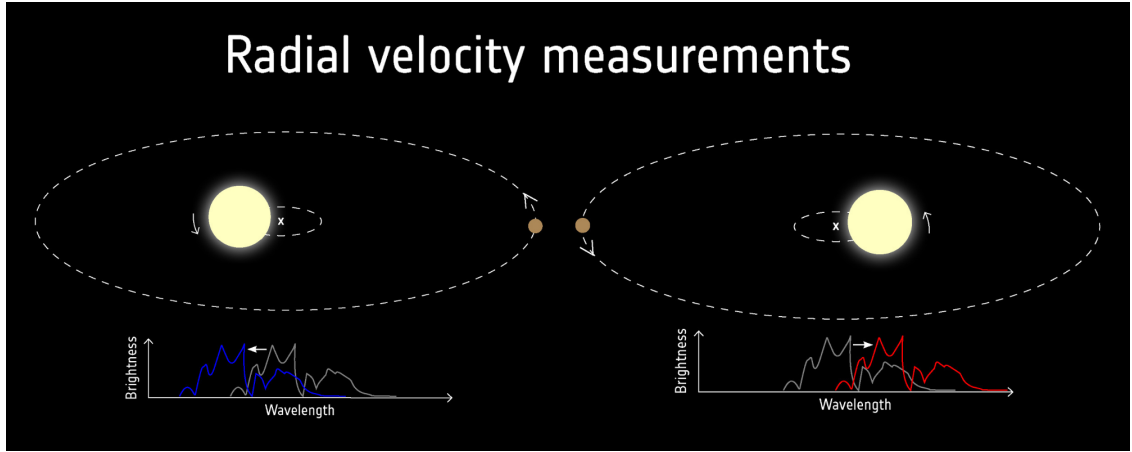


Figure 1: Exoplanets are detectable through the observation of the 'wobble' in their star's motion induced by the gravitational pull of the planet as both orbit a common center of mass. When observed from a distance, the star exhibits an apparent motion towards and away from the observer. This motion causes a slight blue shift in the star's light when moving towards the observer and a slight red shift when moving away. This change in frequency is referred to as the Doppler effect, analogous to the change in pitch of an ambulance siren as it passes by. Credit: ESA⁵

After obtaining both the radius and the mass, we calculate the bulk density using the straightforward equation:

$$\rho = \frac{M_p}{\frac{4}{3}\pi R_p^3} \quad (3)$$

Ultimately, utilizing the average density, which serves as our primary - and only real - tool, alongside the planet's mass and radius, we can try to ascertain the entire composition of the planet interior⁶ (see section 2).

Now that we have identified our primary targets for observation, the M dwarfs, and have established the methodology for exoplanet detection, let us turn our attention to the specific types of exoplanets on which we will focus.

1.3 Exoplanets classification

While one option might be to concentrate on larger, hotter exoplanets known as Hot Jupiters, which are similar to gas giants like Jupiter and Saturn, these planets are not considered optimal candidates for hosting life or habitable conditions. This is because they have very short orbital periods (less than 10 days), placing them very close to their host stars, typically within 0.1 AU[17]. This proximity leads to very high surface temperatures, so high it is unlikely for water, a key ingredient for life as we know it, to exist in liquid form on these planets[18].

Instead, we are going to focus our study on smaller exoplanets that are much more promising and intriguing, such as Super-Earths, sub-Neptune planets, and their subcategory, the Hycean worlds.

⁶Source: <https://physics.mit.edu/wp-content/uploads/2021/01/physicsatmit08seager.pdf>

1.3.1 Super-Earths and sub-Neptune planets

Planets between the size of Earth and Neptune (with radii of $1\text{--}4 R_{\oplus}$) are the most common class in our galaxy but have no analog in our solar system. Spanning a wide range of possible interior and atmospheric compositions, they usually orbit closer to their host stars than Mercury does the Sun[19].

These small exoplanets are currently categorized into two main groups: those smaller than approximately $1.7 R_{\oplus}$ are labeled as super-Earths and are believed to have terrestrial characteristics with iron-to-silicate ratios similar to those of Earth and Venus. On the other hand, those with radii between $1.7\text{--}4 R_{\oplus}$ exhibit bulk densities consistent with a mix of iron, rock, ice, and volatile materials. These exoplanets in the latter category are known as sub-Neptunes or gas dwarfs, as their compositions likely include significant amounts of low mean molecular weight materials such as hydrogen and helium to account for their bulk densities[20]. A substantial hydrogen/helium atmosphere may constitute only a small fraction of a sub-Neptune's total mass, yet it can contribute significantly to its observed radius[21].

There is an interesting relative under abundance of Sub-Neptune planets between 1.5 and $2.0 R_{\oplus}$, often referred to as the 'small planet radius gap'[22]. This bi-modality suggests that sub-Neptunes are primarily rocky planets that initially acquired primary atmospheres, accounting for a few percent of their total mass, from the protoplanetary nebula. Planets above the radius gap were able to retain their atmospheres, classified as "gas-rich super-Earths," while those below the radius gap lost their atmospheres and became stripped cores, known as "true super-Earths." The mechanism responsible for atmospheric loss in these planets remains an unresolved question, with photoevaporation and core-powered mass loss being the leading hypotheses[19]. Although the term "gap" might suggest a complete absence, it does not denote a range of radii entirely missing from the observed exoplanet population. Instead, it signifies a range of radii that are relatively infrequent[22].

1.3.2 Hycean worlds

Now let's delve into a novel category of temperate sub-Neptunes, potential candidates for habitability, characterized by water-rich interiors hosting extensive oceans beneath hydrogen-rich atmospheres: the Hycean worlds, a term derived from "Hydrogen" and "Ocean"[23]. With densities ranging between those of rocky super-Earths and more extended mini-Neptunes, their radii can reach up to $2.6 R_{\oplus}$ ($2.3 R_{\oplus}$) for a mass of $10 M_{\oplus}$ ($5 M_{\oplus}$). Similar to many exoplanets, they may be tidally locked, resulting in the existence of "dark Hycean" planets, habitable only on the side of perpetual night, or "cold Hycean" planets, where minimal irradiation is counterbalanced by the greenhouse effect to maintain warmth. Dark Hycean worlds may arise when atmospheric heat transport from the permanent day side to the permanent night side is ineffective, resulting in temperate temperatures on the night side while the day side is too hot to sustain life[23].

Given the complexity of the classification, determining the true nature of these small exoplanets is challenging due to the degeneracy of their interior. While we can measure their radii and masses, these values only yield a bulk density.

One planet that has likely generated the most debate regarding its true nature is K2-18b.

1.4 Our study case: K2-18b

K2-18b is an exoplanet discovered in 2015 by the team led by Björn Benneke, using data collected by NASA's Kepler Space Telescope employing the transit method[24], later confirmed with the Spitzer Space Telescope through Doppler velocity techniques[25]. It is located approximately 124 light-years away from Earth and orbits a nearby M2.5 dwarf called K2-18 (receiving virtually the same stellar insolation as Earth)[24].

In terms of size, K2-18b has a radius of $R_p = 2.610 \pm 0.087 R_\oplus$ [26], a mass of $M_p = 8.63 \pm 1.35 M_\oplus$ [27] and a bulk density of $2.67^{+0.52}_{-0.47} \text{ g.cm}^{-3}$ [26].

Its orbit lies within the habitable zone of its host star, indicating that the planet could potentially harbor liquid water on its surface and more than this K2-18b abor an intriguing promising atmospheric composition.

Recent observations by the James Webb Space Telescope (i.e., JWST[28]) reveal strong evidence for CH₄ and CO₂ in an H₂-rich atmosphere but did not detect NH₃, H₂O, or CO (see Figure 2).

This offers three possible compositional scenarios for K2-18b according to Nikku Madhusudhan, Matthew C. Nixon et al: a gas-rich mini-Neptune, a Hycean world, or a rocky planet[29].

Madhusudhan et al. 2023 argued that the data are most consistent with a habitable Hycean world[28] because, based on previous photochemical studies, such a planet can align with the absence of NH₃ detection[30] [31] [32] and their retrieved 1% abundances for CH₄ and CO₂ are broadly consistent with predictions made by Hu et al. (2021)[30]. In contrast, ammonia is expected on a mini-Neptune with a substantial hydrogen atmosphere[30] [32].

However, our objective here is to use our model to determine which scenario is most fitting, incorporating both the available internal and atmospheric data.

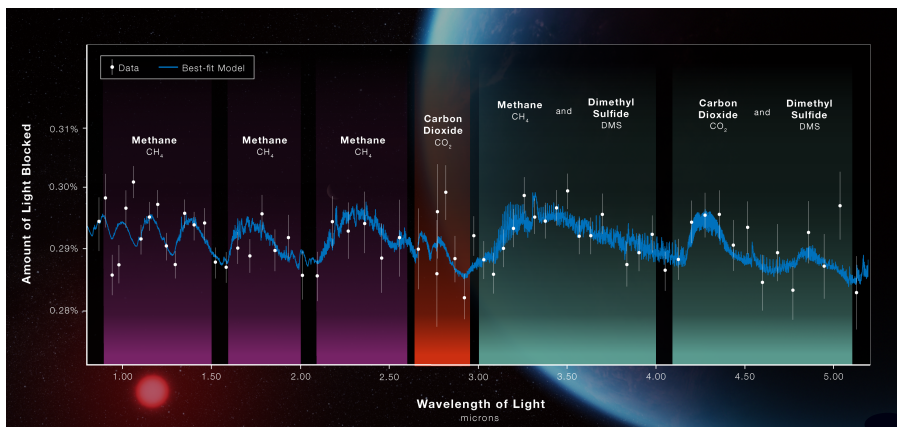


Figure 2: Transmission spectrum of K2-18b atmosphere, obtained with Webb's NIRISS (Near-Infrared Imager and Slitless Spectrograph) and NIRSpec (Near-Infrared Spectrograph) displays an abundance of methane and carbon dioxide in the exoplanet's atmosphere, as well as a possible detection of a molecule called dimethyl sulfide (DMS). Credit⁷: NASA, ESA, CSA, Ralf Crawford (STScI), Joseph Olmsted (STScI)

2 Internal composition constraints

Models are essential tools for enhancing our comprehension of exoplanet characteristics, constructed from observable data related to exoplanets (e.g. mass, radius, orbits, and atmosphere spectra), host stars (e.g. luminosity and chemical composition) and protoplanetary disks (e.g. structure and composition)⁸.

2.1 Formation

We all agree that the condensation of solid materials from stellar nebulae significantly influences the basic composition of planetary building blocks. However, when attempting to understand the formation of sub-Neptune and super-Earth planets, relying on the solar system's formation model - our best-known model - we have a problem due to the absence of such planets in our system [19]. Moreover, the diverse metallicity and metal-to-oxygen ratios observed in extrasolar systems suggest variations in condensation identity, abundance, and sequence compared to our solar system. Consequently, planets forming at similar distances from their host stars may possess compositions distinct from those of the terrestrial planets in our solar system⁸. Hence, we must explore beyond our familiar framework and adjust our perspective. Several potential solutions to this highly pertinent issue have been suggested (for an in-depth examination, see Raymond, Izidoro, & Morbidelli, 2018[33]). Another problematic aspect of constraining the interior of exoplanets through modeling their formation is that we primarily rely on their overall characteristics, such as bulk density, to model their formation. This reliance creates a circular problem where we end up using the information we are trying to understand to build the models themselves.

2.2 Host star

Exploring alien worlds through their stars can provide valuable insights into exoplanet composition. We can not only analyze mass-radius relationships of the planets to know its possible interior structure we also need to consider the composition of the planet's host star. Since planets and their host stars originate from the same system, they share similar material from the accretion disk[34] [35], like similar fractions of certain elements. The iron abundance of a system is particularly crucial, as it is a common component in planetary interiors, along with elements like nickel and metallic alloys[36]. Iron, a relatively heavy element, is believed to be universally present in rocky planets. It can exist in the mantle as silicates and oxides if oxidized, or form the core of a terrestrial planet as a metal. Therefore, the availability of oxygen, along with similarities in mass and radius to known rocky planets, can indicate the possibility of a mantle with oxidized iron[37]. Additionally, the chemical composition of rocky exoplanets can be estimated by measuring the elemental abundances of their host stars and applying a devolatilisation algorithm. This approach, pioneered by Wang et al. (2018, 2019a)[38] [39], considers that rocky exoplanets are likely devolatilised pieces of the stellar nebulae from which they and their host stars formed. Recent research emphasizes the importance of

⁸Source: <https://quanz-group.ethz.ch/research/models-simulations/planetary-composition.html>

applying devolatilisation to the bulk composition of planet-hosting stars, alongside planetary mass and radius measurements, to better understand the interiors of terrestrial-type exoplanets⁸.

2.3 Structure

Here, we will discuss the overall chemical composition and the layered structure of Sub-Neptune and super-Earth planets. Although these two types of planets differ in size and mass, they are believed to share similarities in their formation and composition.

Within the Solar System, rocky planets have a mantle and crust containing silicates, oxides, and silicate melts, and an iron-rich core. The principal elements that compose rocky planets - magnesium, iron, oxygen, carbon, and silicon - are assumed to be universal in the interiors of these planet types, and the abundance of these elements will determine the planet's final composition⁹.

On the other hand, the thickness of a planetary crust is directly proportional to how quickly the planet cooled after its formation. A fast cooling rate is expected for a smaller planet, a low-mass planet, or a planet that is further away from its star. Such planets would have a proportionally thicker crust, as is seen in the Moon and Mars[40]. However, accessing the complete thermal evolution of exoplanets remains challenging.

Confirm unambiguously that an exoplanet is an hycean planet or a rocky planet surrounded by H/He atmosphere remains challenging, as such worlds could occupy the same region of the mass-radius plane, like K2-18b (see Figure 3). Nevertheless, for K2-18b its size and density (see section 1.4) suggest it cannot be composed of only iron and silicate rock as you can see on Figure 3, further investigation on the nature of K2-18b will be described in the section 5.

⁹Source: https://en.wikipedia.org/wiki/Exoplanet_interiors

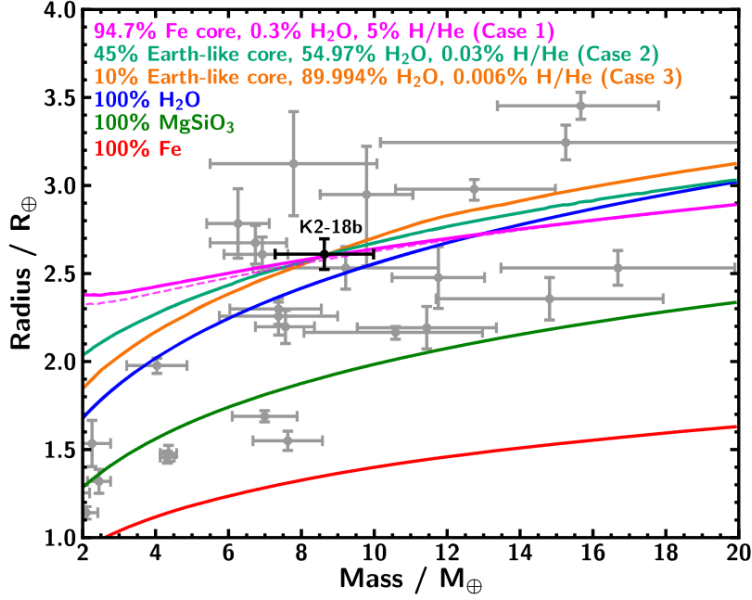


Figure 3: Mass–Radius relations for planets with different compositions. The mass fractions are shown in the legend. The solid magenta, teal, and orange curves show cases that all fit the mass and radius of K2-18b equally well. The dashed magenta line represents the same composition as the solid magenta line but with a mixed H₂O–H/He envelope. Also shown are exoplanets whose masses and radii are known to 3σ with $T_{eq} \leq 1000K$, from TEPCat[41]. Credit: Madhusudha et al. 2020[29].

2.4 Atmosphere

The study of exoplanet atmosphere can help us understand the deeper interior layers of an exoplanet. The connection between the atmosphere and the interior layers of a planet includes processes like volcanism, chemical reactions at the surface, evaporation of the surface in extremely hot conditions, or weathering cycles. The James Webb Space Telescope (JWST) is opening a new window in our ability to characterize exoplanet atmospheres by determining their composition, temperature, and dynamics.

To obtain the spectra of an exoplanet, we observe it as it passes in front of and behind its host star from our perspective. During the first transit, a small fraction of the star’s light passes through the exoplanet’s atmosphere before reaching our telescopes. By analyzing this transmitted light spectrum during the transit, we can discern the chemical composition of the exoplanet’s atmosphere and the degree of light transmission is influenced by the atmospheric opacity, density, and temperature see Figure 2. The second transit – when the planet passes behind the star – provides more information, as the planet’s contribution to the total spectrum is hidden, and we only access light from the host star. This allows us to determine which molecules or atoms are from the planet’s atmosphere and which are from the star. The final atmosphere composition allows us to investigate the internal composition of the planet and gain insights into its physical and chemical properties.

For instance, for K2-18b, atmospheric NH₃ depletion can be a natural consequence of the high solubility of nitrogen species in magma under reducing conditions, precisely the conditions prevailing where a thick hydrogen envelope is in

communication with a molten planetary surface. Thus, there is a chance that K2-18b is hosting either an ocean of water or magma. Differentiation between them could be determined by observing a small CO₂/CO ratio in the >4 μm wavelenght region, where CO₂ and CO features dominate, indicating magma[42]. This is why integrating atmospheric spectra into models of the interior and comprehension of chemistry processes are essential. Moreover, the species found in the spectra provide information on the mean molecular weight, influencing planetary radius and mass, as analyzed in Section 6.

Additionally, we do not know how thick the atmosphere of K2-18b is, which is one of the most important problems when it comes to habitable conditions. A small atmosphere is compatible with an underlying ocean, which would be more favorable to life, as we know it on Earth, whereas a massive atmosphere would leave less space for an ocean and would be so dense that it is less favorable for life, similar to Jupiter or Saturn.

3 Models used

Our objective is to develop a new model framework combining the planet interior structure model, **MAGRATHEA**, and a nested sampling algorithm to constrain the mass of each layer for small exoplanets. Instead of specifying the mass of individual layers of the planet, as done in **MAGRATHEA**, the user will input the total mass, total radius, and bulk density of the planet determined through the detection method outlined in a previous section (refer to section 1.2). Our model will then constrain the mass of each potential layer of the exoplanet using a nested sampling algorithm.

3.1 MAGRATHEA

There are numerous methods for modeling the interiors of exoplanets, utilizing a variety of computational techniques, experimental data, temperature profiles, and theoretical equations of state (EOS) for the materials composing these celestial bodies. Here we are presenting and utilizing: **MAGRATHEA**.

MAGRATHEA is an open-source planetary structure code specialized in modeling fully differentiated, spherically symmetric interiors. By inputting layer masses, surface temperature, and the pressure level that the broad band optical transit radius probes, the code employs iterative methods, specifically the shooting method to adjust hydrostatic equations' boundary conditions until it converges to a suitable solution for determining the planet's radius. The user can input up to four layers comprising an iron core, a silicate mantle, a steam/water/ice hydrosphere, and a default H/He atmosphere that can vary in composition. Temperature profiles, including options such as isothermal, isentropic, or custom-defined functions, can also be chosen, with certain restrictions. Furthermore, users can select various phase diagrams, where the EOS may change based on P-T conditions inside each layer, and multiple formulations, both thermal and non-thermal, for the EOS are implemented[2]. This model is available at <https://github.com/Huang-CL/Magrathea>.

The main advantage of **MAGRATHEA** lies in the flexibility offered to the user alongside its rapid convergence compared to other interior models, such as ExoPlex[2], which is useful when employing nested sampling technique that requires significant convergence time.

The name of **MAGRATHEA** comes from the legendary planet where hyperspatial engineers manufacture custom-made planets in Douglas Adams's *The Hitchhiker's Guide to the Galaxy*¹⁰.

3.1.1 Model equations[2]

The model assumes a single solution to composition, at a given pressure and temperature, exists within each layer. The solver returns a planet interior profile file after completion, which includes the r, P, T, m, ρ , and the component phase at each grid step. Given the mass of each of these layers, $M_{\text{comp}} = \{M_{\text{core}}, M_{\text{mantle}}, M_{\text{hydro}}, M_{\text{atm}}\}$, the code calculates the radius returning the pressure $P(m)$, density $\rho(m)$, and temperature $T(m)$ with enclosed mass m by solving the following four equations:

(i) Mass continuity equation

$$\frac{dr(m)}{dm} = \frac{1}{4\pi r^2 \rho(m)} \quad (4)$$

(ii) Hydrostatic equilibrium

$$\frac{dP(m)}{dm} = -\frac{Gm}{4\pi r^4} \quad (5)$$

(iii) Temperature gradient

When the isothermal option is chosen, the temperature gradient is 0. When the isentropic option is chosen, depending on the available thermal properties of the phases, the temperature gradient can be calculated using either of the following two formulae. If the Grüneisen parameter γ is available, we can have :

$$\frac{dT(m)}{dm} = \left(\frac{dT}{dV} \Big|_S \right) \frac{dV}{d\rho} \frac{d\rho}{dm} = -\frac{m_{\text{mol}}}{\rho^2} \left(\frac{dT}{dV} \Big|_S \right) \left(\frac{\partial \rho}{\partial P} \frac{dP}{dm} + \frac{\partial \rho}{\partial T} \frac{dT}{dm} \right). \quad (6)$$

Thus,

$$\frac{dT(m)}{dm} = \frac{\left(\frac{dT}{dV} \Big|_S \right) \frac{Gm}{4\pi r^4}}{\frac{\rho^2}{m_{\text{mol}}} \left(\frac{\partial P}{\partial \rho} \Big|_T \right) - \left(\frac{dT}{dV} \Big|_S \right) \left(\frac{\partial P}{\partial T} \Big|_\rho \right)}, \quad (7)$$

where

$$\left. \frac{dT}{dV} \right|_S = -\frac{\gamma T}{V}, \quad (8)$$

m_{mol} and V are the molar mass and volume respectively. Alternatively, if the thermal expansion α is available, we can have

$$\frac{dT(m)}{dm} = -\frac{\alpha T G m}{4\pi r^4 \rho c_p}, \quad (9)$$

¹⁰Adams D., 1995-2001, *The Hitchhiker's Guide to the Galaxy*. Harmony Books, New York

where c_p is the specific heat capacity at constant pressure.

(iv) Equation of state (EOS)

$$P(m) = P(\rho(m), T(m)) \quad (10)$$

Which is unique for each material/phase. There are over 30 EOSs available in MAGRATHEA which can be called within the phase diagrams, see section 3.1.2. These include EOS functions for various planet building materials, and different parameter estimates for the same material from various works, see section 3.1.3.

The boundary conditions of the model are $r = 0$ at $m = 0$.

3.1.2 Phase diagrams[2]

A phase diagram for each layer is essential as phase transitions may occur due to the extensive pressure and temperature variations within each layer. During computation, the code initially assesses the pressure and temperature to pinpoint the appropriate region on the phase diagram.

One notable aspect of MAGRATHEA is the user's ability to customize the phase diagram in each layer and choose between Equations of State (EOSs) for each phase. This flexibility will allow us to test several compositions for the core, see section 5.0.3.

3.1.3 Chemistry[2]

Here we will discuss the chemistry and the state of matter of the four layers. The generic model comprises an Fe inner core, a rocky (silicate) outer core, an H₂O layer, and an H/He-rich atmosphere.

(i) Core/Iron

At the extreme pressures of a planetary core, iron is stable in a hexagonal close-packed (HCP) phase. For a pure iron core (see section 4) the default equation is the one from Smith et al. 2018[43] measured by ram compressing iron to 1.4 TPa. We can also choose iron-silicate alloy EOSs, for Fe-Si alloys with 7 weight percent Si and 15 weight percent Si from Wicks et al. 2018[44], useful when reproducing the density of the Earth's core which contains an unknown mixture of light elements[45] (see section 5.0.3).

(ii) Mantle/Silicate

The main mineral constituent of the Earth's mantle is bridgmanite (Brg), also known as silicate perovskite which at high pressure transitions to a post-perovskite (PPv) phase[46]. At high temperatures (> 1950 K at 1.0 GPa), the magnesium silicate, $MgSiO_3$, is liquid and the default equation from Wolf and Bower 2018[47] is used. For Bridgmanite/Perovskite the model uses the equation from Oganov and Ono 2004[48] and for Post-Perovskite the equation from Sakai, Dekura, and Hirao, 2016[49]. Our default mantle is thus pure $MgSiO_3$ in high-pressure phases which is more SiO_2 rich than the Earth.

(iii) Hydrosphere/Water

Similar to the icy moons in the Solar System; exoplanets with low density are

theorized to have a large fraction of mass in an hydrosphere composed primarily of high-pressure water-ice. Due to the complexity of the phase diagram of water and large uncertainties in current measurements, in the last version of MAGRATHEA, a simplified hydrosphere phase diagram is used, see Figure 4.

At pressures below 2.216 GPa, the liquid water equation from Valencia et al. 2007a[50] is applied, if the temperature is above the melting curve then the equation from Dunaeva et al. 2010[51] is used. Below the melting curve, there are Ice Ih equation from Feistel and Wagner 2006[52] and Acuña et al. 2021[53] at pressures below 0.208 GPa. For pressures above 0.632 GPa, Ice VI equation from Bezacier et al. 2014[54] is used. Ice II, III, and V, which exist at intermediate pressures, are currently not included as their layers are thin and have a negligible impact on the planet. If a planet passes through these phases, the Ice VI EOS is used and the user is notified that they passed through this region. At high pressure, the default hydrosphere layer uses Ice VII with thermal expansion from [54]. Lastly, the default hydrosphere transitions at 30.9 GPa for Ice X used the equation from Grande et al. 2022[55].

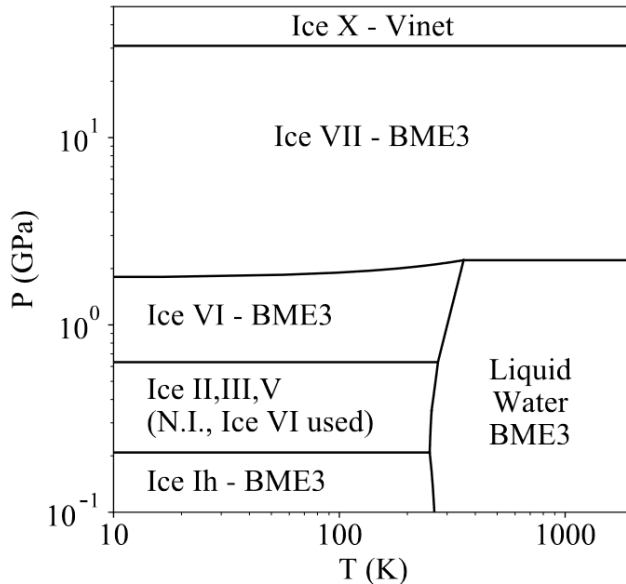


Figure 4: Default log-linear pressure-temperature phase diagram for the hydrosphere. Vinet and BME3 stand for the different EOS used to calculate the reference isotherm pressure P_c for more detail see Huang et al. 2022[2].

(iv) Atmosphere/Gas

The ideal gas equation of state: The following equations are applied to the gas layer at all pressures and temperatures,

$$P = \frac{\rho R T}{m_{mol}} \quad (11)$$

and temperature relation:

$$T \propto P^{\frac{\gamma_{gas}-1}{\gamma_{gas}}} \quad (12)$$

Where γ_{gas} is the adiabatic index of the gas, and we have the ideal gas temperature gradient:

$$\frac{dT(m)}{dm} = -\frac{(\gamma_{gas} - 1)m_{mol}Gm}{4\pi r^4 \gamma_{gas} R \rho} \quad (13)$$

To simulate this temperature structure, the default settings for the atmosphere in MAGRATHEA include an isothermal atmosphere at $P < 100$ bar to approximate the radiative temperature gradient, and an adiabatic temperature gradient at $P \geq 100$ bar.

The mean molecular weight of each gas EOS can be changed to allow us to explore atmospheres with different compositions as described in section 5.0.2.

3.2 UltraNest

As we mentioned, our goal is to constrain up to four parameters corresponding to the masses of each layer of the planet we are examining. Different techniques have been developed to explore model parameter spaces, but we chose to focus on the nested sampling technique called UltraNest.

Nested sampling is a powerful statistical technique used to sample from complex probability distributions, particularly useful in Bayesian inference. It works by iterative sampling from the prior distribution while progressively narrowing down the region of interest in the parameter space. This technique allows for efficient exploration of the parameter space by focusing computational effort on the most probable regions, which is especially advantageous when dealing with high-dimensional or multimodal distributions. By continuously updating the nested regions, this method provides a robust estimate of the evidence and posterior distributions, making it ideal for our purpose of constraining the masses of planetary layers.

UltraNest employs a combination of active point clustering and ellipsoidal bounding to efficiently explore the parameter space and accurately estimate the evidence. By adaptively allocating computational resources to regions of high likelihood, UltraNest achieves faster convergence and better performance compared to traditional MCMC (Markov Chain Monte Carlo) methods, especially for challenging problems with multimodal or highly correlated posterior distributions,¹¹ which is our case. For a more detailed look on the convergence method see <https://johannesbuchner.github.io/UltraNest>

In the following section, we are going to discuss the choices made to archive our goal.

4 Our model

4.1 Environment

Firstly, we adapt the MAGRATHEA code, originally written in C++, into Python by creating a Python wrapper¹². This new code allows for greater flexibility and accessibility, as Python is widely recognized for its simplicity and intuitiveness of use. This transition also opens doors for the use of other Python-based tools and frameworks, such as the `ultranest` package¹³.

¹¹Source: <https://johannesbuchner.github.io/UltraNest/readme.html>

¹²Source: <https://www.geeksforgeeks.org/function-wrappers-in-python/>

¹³Source: <https://pypi.org/project/ultranest/>

To do so we use Visual Studio Code¹⁴ on Ubuntu¹⁵ under WSL (Windows Subsystem for Linux)¹⁶.

When wrapping **MAGRATHEA**, we keep the output as a file containing the six different parameters of each step of the simulation (see section 3.1.1). We choose to display the values of the bulk density (in $g.cm^{-3}$), the final mass (in M_{\oplus}), and the final radius (in R_{\oplus}), as those are the parameters that we will use in the log-likelihood function (see section 4.3.2).

4.2 Inputs

The main inputs in our code are the total mass, total radius, and bulk density of the exoplanet we want to constrain the composition and their uncertainties associated as presented below (K2-18b parameters):

Obs_Mass = 8.63	Err_Mass_Max = 1.35	Err_Mass_Min = 1.35
Obs_Rad = 2.610	Err_Rad_Max = 0.087	Err_Rad_Min = 0.087
Obs_Dens = 2.67	Err_Dens_Max = 0.50	Err_Dens_Min = 0.50

In addition, other inputs are the surface temperature of the planet, for instance, 284.0 K [56] for K2-18b, and the pressure level that the broad band optical transit radius probes, which corresponds to the pressure range that the measuring instrument is capable of probing. This value is set to 100 μ bar and will remain fixed throughout the entire project, as it is an accurate value for K2-18b and sub-Neptunes in general.

Future parameters that we will test, such as the mean molecular weight of the atmosphere and the core EOS (see Section 5), will be directly modified in the C++ code of **MAGRATHEA**.

In the model, we can set how many, and which, layers we want to include in our planet, corresponding to the parameters to fit in our nested sampling algorithm. M1 corresponds to the mass of the core, M2 to the mass of the mantle, M3 to the mass of the hydrosphere, and M4 to the mass of the atmosphere. For instance, if there is no observed atmosphere, we can set the M4 parameter to zero. If we aim to test a rocky planet with an ocean, we can retain only M1 and M3.

Now that all the inputs are well defined we are creating the nested sampling algorithm.

4.3 UltraNest algorithm

4.3.1 Prior fonction

First, we need to convert the parameters to physical scales using a cube function. The cube function takes arguments ranging from 0 to 1. Through this function, we can determine the range explored for each model parameter. This can be done either by fixing the range based on the maximum mass of the planet for each parameter, which is useful when you have no prior idea of the final mass for each layer, or by preconstraining a range of values for each parameter.

¹⁴Source: <https://code.visualstudio.com/>

¹⁵Source: <https://ubuntu.com/>

¹⁶Source: <https://learn.microsoft.com/en-us/windows/wsl/>

For example, in the case of K2-18b, based on its position on the Mass-Radius diagram (Figure 3), we know that all the mass cannot be in the core. Therefore, we can set an upper boundary where a maximum of 80% of the mass is allocated to the core. The cube function operates as follows:

```
params[0] = cube[0] * max_value_for_param_0
params[0] = cube[0] * 7.984
```

Here, the index in params and cube is 0 because we constrain the core, which is the first layer, but since the index starts at 0 in Python, it will be the first one. The max_value_for_param_0 in this case corresponds to 80% of the (Obs_Mass + Err_Mass_Max) of K2-18b. In reality, the final nested sampling algorithm automatically rules out the case of a full iron core for a planet like K2-18b, due to the next function, the log-likelihood function. This preconstraint on mass is useful when the user wants to force the model to try a specific composition range. Otherwise, no preconstraint is needed, and the range for each parameter is equal to the total mass of the planet.

4.3.2 Log-likelihood

The Log-likelihood function is one of the most important parts of the model, as it is this function that determines the accuracy of our predictions.

We tried different formulations to minimize the final value of this function, as the log-likelihood variable calculates how far the data are from the model predictions. More precisely, this function calculates how often the observed data would arise under the given parameters, so the goal is to bring this function closer to zero. Here, we are going to discuss some of the strategies we tried and the conclusions that were drawn.

First, taking as input the four previously transformed parameters, we run the wrapped **MAGRATHEA** with total random parameters - still within the range defined in the prior function. The values returned are called: Mod_Mass, Mod_Rad, and Mod_dens.

We assume a Gaussian model and measurement errors of known size (Err_Mass_Max and Err_Mass_Min):

My first strategy was to try a basic Gaussian model, constraining only the total mass:

$$\text{loglike} = -0.5 \times \left(\frac{\text{Mod_Mass} - \text{Obs_Mass}}{\max(\text{Err_Mass_Max}, \text{Err_Mass_Min})} \right)^2 \quad (14)$$

However, no convergence was achieved even for only two parameters. So, instead of modeling the mass only, we tried to add the contribution of the radius to the function to be more constraining and as the bulk density combines both the radius and the mass parameter, we chose to use its contribution instead.

$$\text{loglike} = -0.5 \times \left(\frac{\text{Mod_Dens} - \text{Obs_Dens}}{\max(\text{Err_Dens_Max}, \text{Err_Dens_Min})} \right)^2 \quad (15)$$

The convergence was slightly better but still not there. Then we tried to penalize the function when it was going too far above the value of (`Obs_Dens + Err_Mass_Dens`) or below the value of (`Obs_Dens + Err_Dens_Min`):

```
if Mod_Dens < (Obs_Dens - Err_Dens_Min) :
    loglike = -1 * 10-99
elif Mod_Dens > (Obs_Dens + Err_Dens_Max) :
    loglike = -1 * 10-99
else :
    loglike = Equation 15
```

Once again, nothing more conclusive. The penalties were probably too high. So, we added an adaptive penalty that will be high when the model is far from the observed value and will decrease as we approach the correct value. To do this, we are taking the absolute value of the difference between my model and the observed value, and we choose a lambda parameter that will define the degree of penalty.

```
abs_diff_dens = np.abs(Mod_Dens - Obs_Dens)
penalty_dens = λ * abs_diff_dens
```

This was working much better. We tried many different values for lambda, and the best one was 0.5, as it was the one giving the smallest uncertainties. This is the value we are going to use for the rest of the project.

As we will later discuss in Section 4.5.2, the high degeneracy of this modeling required the inclusion of the contribution of three main parameters penalties. The final and best log-likelihood function was then:

$$\text{loglike} = -0.5 \times \left(\frac{\text{Mod_Dens} - \text{Obs_Dens}}{\max(\text{Err_Dens_Max}, \text{Err_Dens_Min})} \right)^2 - \text{penalty_dens} - \text{penalty_mass} - \text{penalty_rad} \quad (16)$$

with the three penalties being formulated the same as `penalty_dens`.

4.3.3 Global parameters

Finally, we need to define the minimum number of "live points" (`min_num_live_points`) that the algorithm must maintain throughout the sampling process. In principle, selecting a very low number enables nested sampling to quickly reach the peak with minimal iterations. However, this approach results in poor sampling of the space, leading to a large region with low efficiency and the potential to miss interesting modes. Consequently, a value above 100 is generally recommended, with 400 being a good initial choice, which is the value we selected.¹⁷

¹⁷Source: <https://johannesbuchner.github.io/UltraNest/issues.htmlhow-should-i-choose-the-number-of-live-points>

We set the Kullback-Leibler divergence (dKL) to infinity, deactivating any potential stopping criterion.

The last parameter to set is the minimum effective sample size, ESS, called 'min_ess' in our model. It represents the minimum number of effective samples that the algorithm must obtain before stopping. Its function is to measure the quality of the samples obtained, taking into account the correlation between them. A higher ESS means that the samples are more independent and therefore of better quality. We are selecting 10 as a starting point; although this value is low, it allows us to quickly detect any issues with the simulation.

4.4 Outputs

While running the model, the user will be able to see the live progression of the model constraints on the parameters. Once the model is done, the result of the convergence will be displayed through a corner plot diagram, showing the distribution of each variable on the diagonal and the relationships between pairs of variables in the off-diagonal plots. This helps visualize individual distributions and correlations in a dataset and provides the best value for the mass of each layer and their associated uncertainties, the narrower the Gaussian shape of the model's parameters, the fewer uncertainties we will have (see left Figure 5 for example). We also have access to the final value of the loglike function, which is useful when comparing the possible different interior compositions for a same planet (see section 6). The second plot we created is a pie slice chart of the planet's mass distribution based on the result of the model to make it more intuitive and clear. This plot also shows the recalculated values of total mass, radius, and bulk density, as determined by MAGRATHEA, using the mass results from our simulation. Then it highlights the differences between the initial input values and those obtained from the simulation results (see right Figure 5 for example).

4.5 Benchmark tests

For further understanding of the model, benchmark tests are required.

4.5.1 Two-layer planet

We are first testing the model by simulating a fake planet with a simple composition of $0.3M_{\oplus}$ of iron and $0.7M_{\oplus}$ of silicate, an Earth-like case to test our model. We start with two layers for the model to constrain. We use the default phase diagrams and equations of state for the iron core and magnesium silicate mantle. We are fixing the temperature to 300K and we assume thermal equilibrium between each boundary layer. The pressure, as always, is fixed to $100\mu\text{bar}$.

As this test will serve to 'benchmark' the model, we need to know what we are looking for, both the input and the output. To do so, we are using MAGRATHEA first; for the above values, the model is giving (rounded to three significant figures):

- Final Mass: $1.000M_{\oplus}$
- Final Radius: $0.974R_{\oplus}$
- Bulk density: $5.946g.cm^{-3}$

We can now run our model by inputting the total mass, radius, and density above, fixing an arbitrary uncertainty of 0.05 for each parameter. We are running the model without any prior information on the two mass parameters to retrieve, except that there are between 0 and $1M_{\oplus}$ using the log-likelihood function with λ of 0.5, and using the global parameters established in section 4.3.3. The results of this simulation are shown in Figure 5 below:

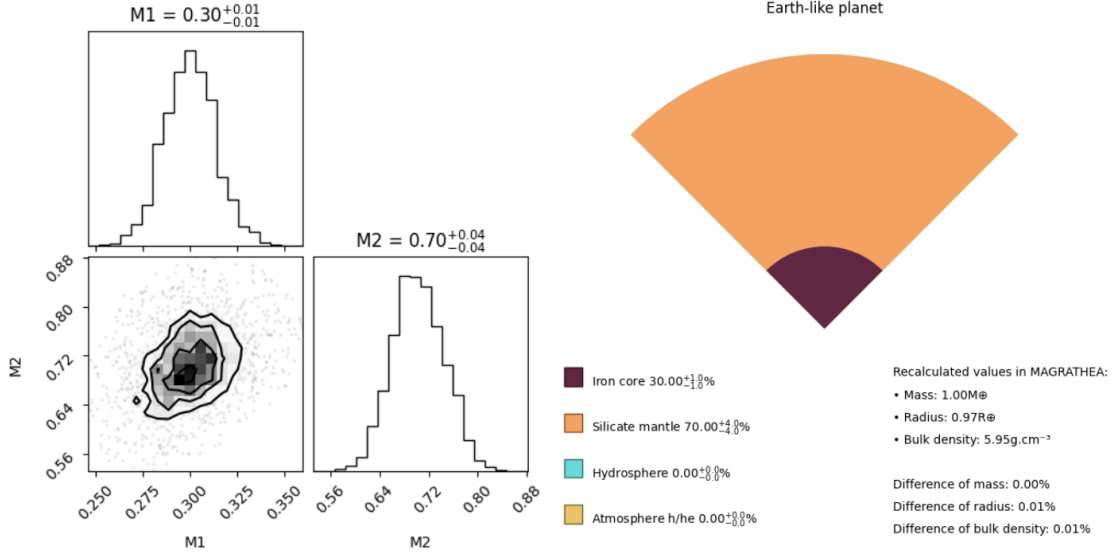


Figure 5: Output plots showing the results of the simulation, the first plot is showing the corner plot results of an earth-like planet simulation with two-layer and the second plot shows the mass distribution and the difference between the simulation and the initial values.

It can be seen that in the first plot, the values are quite accurate, and the uncertainties are consistent with the initial one. In the second figure, when we re-input the algorithm’s results into MAGRATHEA, which calculates the new total mass, radius, and bulk density, the difference from the initial input is small. Although we cannot precisely quantify the significance of this value due to the exclusion of uncertainties in the calculation, this small difference, along with the current uncertainties we obtained, is quite satisfactory.

It is important to note that when we increase the initial uncertainties, the model’s accuracy decreases. By adjusting the parameter λ , we found that the best results are achieved with $\lambda = 0.5$.

For a two-layer planet, the expected results are always retrieved but depend strongly on the initial predictions, initial values, and the complexity of the model. Indeed for an Earth-like planet, the final uncertainties are the lowest, which is logical because the EOS of MAGRATHEA are based on Earth’s characteristics.

4.5.2 Three-layer planet

Here we are doing the same thing as we did for the two layer planet but we are adding an atmosphere. We are choosing an atmosphere with a mass of $0.3M_{\oplus}$ and we are recalculating the total parameters value through MAGRATHEA by inputting $M_{tot} = \{0.3, 0.7, 0, 0.3\}$ here are the results (rounded to three significant figures):

- Final Mass: $1.300 M_{\oplus}$
- Final Radius: $1.803 R_{\oplus}$
- Bulk density: $1.219 g.cm^{-3}$

We are following the same process as for the two-layer planet, keeping the same global parameter values and assumptions. Here are the two resulting plots:

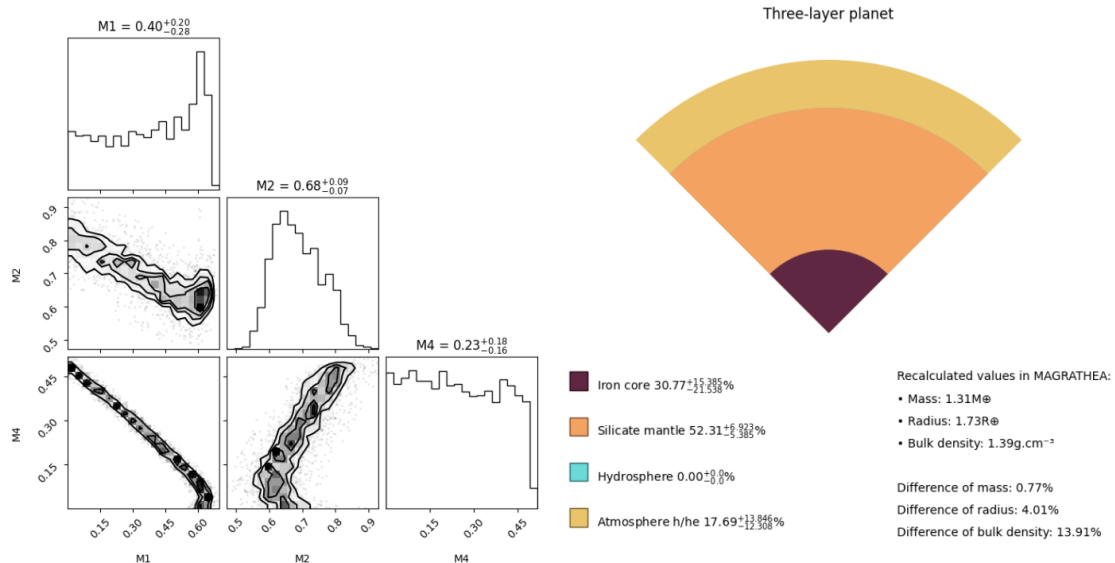


Figure 6: Output plots showing the results of the simulation, the first plot is showing the corner plot results of a three-layer planet and the second plot shows the mass distribution and the difference between the initial value and the simulation.

As discussed in Sections 1 and 2, the degeneracy among potential composition scenarios presents our main obstacle. This ambiguity becomes particularly evident when attempting to constrain three layers simultaneously. As illustrated in left Figure 6, the uncertainties are larger than for a two-layer planet, and the model struggles to converge, resulting in a degenerate solution. The relationship between the parameters appears linear, indicating that as the mass of the core increases, the masses of the atmosphere and the mantle will decrease. This is why most papers on modeling the interiors of exoplanets focus on fixing one or two layers while attempting to retrieve the others[29], as we plan to do in Section 4. When encountered this problem, we tried to incorporate the contributions of radius and mass into the log-likelihood function to better discriminate the mass of each layer. However, it turns out that this approach led to worse results, likely because these contributions were already accounted for in the density calculation.

However, we can still observe that the mantle is relatively well-constrained. Being the middle layer, the model can converge to a better value as it takes into account the constraints on the surrounding layers plus its own.

Nevertheless, the model's final values agree still well with the observed values (see difference values on the right Figure 6). However, these values are not particularly pertinent in this test case since we know what we need to retrieve. It will be more interesting in the case of K2-18b (see Section 5).

4.5.3 Four-layer planet

The final step we need to attempt is to constrain all four layers simultaneously, which would lead to the most accurate modeling of the interior due to increased flexibility in the model. However, as seen with the three layers, it is predictable that the degeneracy between the different scenarios will make this task almost impossible. Therefore, we are trying and repeating the operation once again, adding the last available layer: a hydrosphere of $0.4 M_{\oplus}$. Then we are following the same process as for the two and three-layer planet, keeping the same global parameter values and assumptions.

The simulation never converged, indicating that there is too much degeneracy for convergence as all parameters depend completely on each other. Therefore, the conclusion is that we will stick to constraining only two layers simultaneously, which still leaves a range of possible interiors as we will later change the composition within a layer.

4.6 Other parameters

In addition to adjusting the number of layers, we can also modify parameters within the algorithm. Two particularly noteworthy parameters are temperature and the number of live points.

- Temperature:

Increasing the temperature will elevate the mass of the upper layers of the planet while reducing the mass of the inner layers. It will indeed extend the total radius of the planet, thus reducing the bulk density.

- Min_num_live_points:

Increasing the number of live points slows down the convergence of the simulation but enhances the accuracy of the constraints.

5 K2-18b case

In this part, we are going to focus on K2-18b, trying to constrain its internal composition as accurately as possible by considering different interior possibilities.

To do so, we provide the model with the total mass, radius, and density along with their associated uncertainties from Section 1.4, and we change the surface temperature to 284.0 K [56].

5.0.1 Main composition

As we concluded in the previous section, we need to fix two layers to have a more accurate constraint on the other two. We are going to perform two tests to determine which layer is favored by the model.

For the first simulation, the core and the mantle of the planet are fixed. We choose an Earth-like core and set the mantle to zero. On Earth, the core accounts for approximately 32% of the total mass. Therefore, we fix $M_1=2.7616M_{\oplus}$ and

$M_2=0$, then we try to retrieve the mass of the hydrosphere and atmosphere. We keep the same assumptions as in Section 4.5 and run the model. The results are shown in Figure 7, and the differences between the model and the observed values, plus the result of the loglike value are given in Table 1.

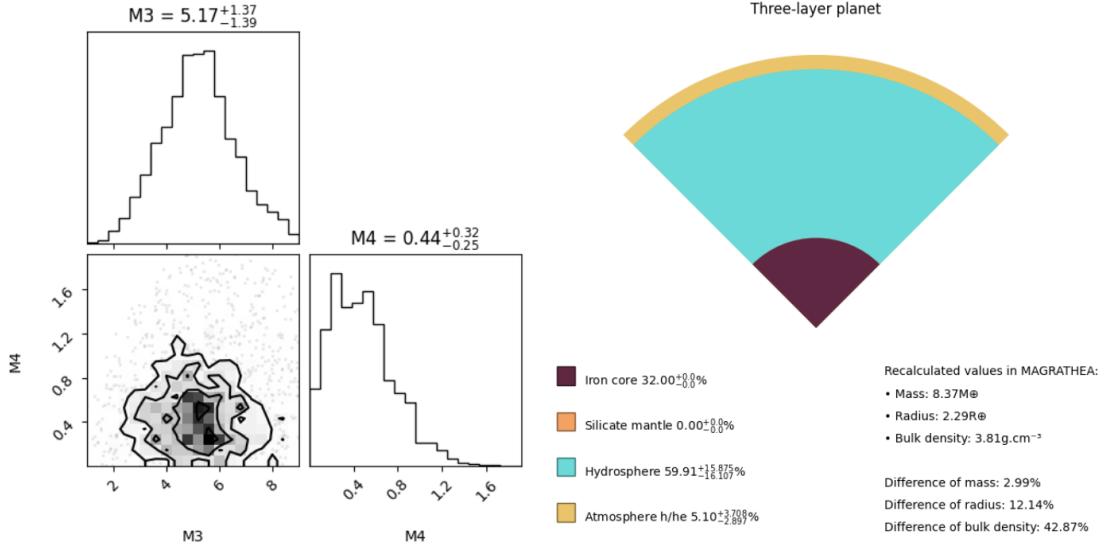


Figure 7: Output plots showing the results of the simulation. The first plot displays the corner plot results of a three-layer planet with a core, hydrosphere and atmosphere. The second plot shows the mass distribution and the difference between the initial value and the simulation.

For the second simulation, we are still fixing the core mass to $M_1=2.7616M_{\oplus}$ and we are choosing a hydrosphere equivalent to the amount of water on Earth, which is 0.02% of the total mass¹⁸. This corresponds to $M_3=0.1726M_{\oplus}$ for K2-18b. We then model a mantle and an atmosphere. The results are shown in Figure 8, and the differences between the model and the results are given in Table 1.

¹⁸Source: <https://phys.org/news/2014-12-percent-earth.html>

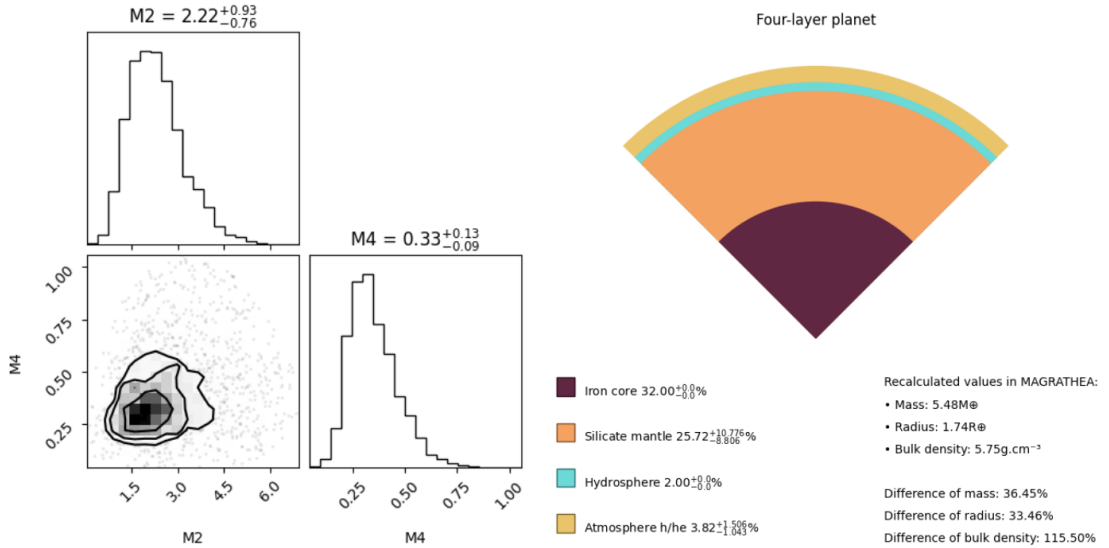


Figure 8: Output plots showing the results of the simulation. The first plot displays the corner plot results of a four-layer planet. The second plot shows the mass distribution and the difference between the initial value and the simulation.

The results reveal that the three-layer planet exhibits smaller differences between the model predictions and initial values compared to the four-layer planet, suggesting a closer direct match. This could be attributed to the simpler modeling approach of the three-layer system, potentially leading to fewer deviations. However, in contrast, the four-layer planet shows better constrained layers, characterized by a more defined Gaussian shape and reduced final uncertainty. This underscores the inherent trade-off between achieving accuracy in raw differences versus the precision of the model’s predictions.

Moving forward, we will focus exclusively on a three-layer planet with a core, hydrosphere, and atmosphere, as this model facilitates a clearer understanding of planetary mass distribution and generally provides more accurate results.

5.0.2 Atmosphere

As we have access to the transmission spectra of K2-18b (see Figure 2), we will include the contribution of the molecules present in its atmosphere to understand their impact on the rest of the interior composition. To achieve this, we will calculate and adjust the value of the mean molecular weight in the MAGRATHEA code.

The concentration of each molecule in the atmosphere is primarily influenced by chemical processes, wind-driven mixing, and condensation. These three processes vary across different regions of the atmosphere. Utilizing the mean molecular weight constraints from JWST observations provides a useful first-order approximation for the input needed to model the atmospheric layer composition. The spectral features of hydrogen and helium are not visible because these neutral gases do not have absorption features in the observed wavelength range. Nevertheless, their presence in the atmosphere is inferred from their significant contribution to the mean molecular weight, which enhances the spectral signatures of other gases’ absorption.

To determine the final mean molecular weight, we start by measuring the amplitude of the two main spectral features, CH₄ and CO₂, to evaluate their contri-

bution to the total mean molecular weight. Using equation (11) and the known amplitudes, we calculate their approximate contribution, denoted as f in percentage. The remaining percentage is attributed to the hydrogen and helium mix. Here, M_X represents the molar mass in g.mol⁻¹ of each species X .

$$\begin{aligned} M_{\text{moy}} &= (f_{\text{CH}_4} \cdot M_{\text{CH}_4}) + (f_{\text{CO}_2} \cdot M_{\text{CO}_2}) + (f_{\text{H/He}} \cdot M_{\text{H/He}}) \\ &= (0.275 \cdot 16) + (0.250 \cdot 44) + (0.475 \cdot 3) \\ &= 16.825 \text{ g.mol}^{-1} \end{aligned} \quad (17)$$

We find a value of 16.825 g.mol⁻¹ and thus we change the original value of 3 g.mol⁻¹ to this new one.

We are still fixing an Earth-like core and also the mantle to zero. The result are shown in the Figure 9 and the likelihood value is provided in Table 1.

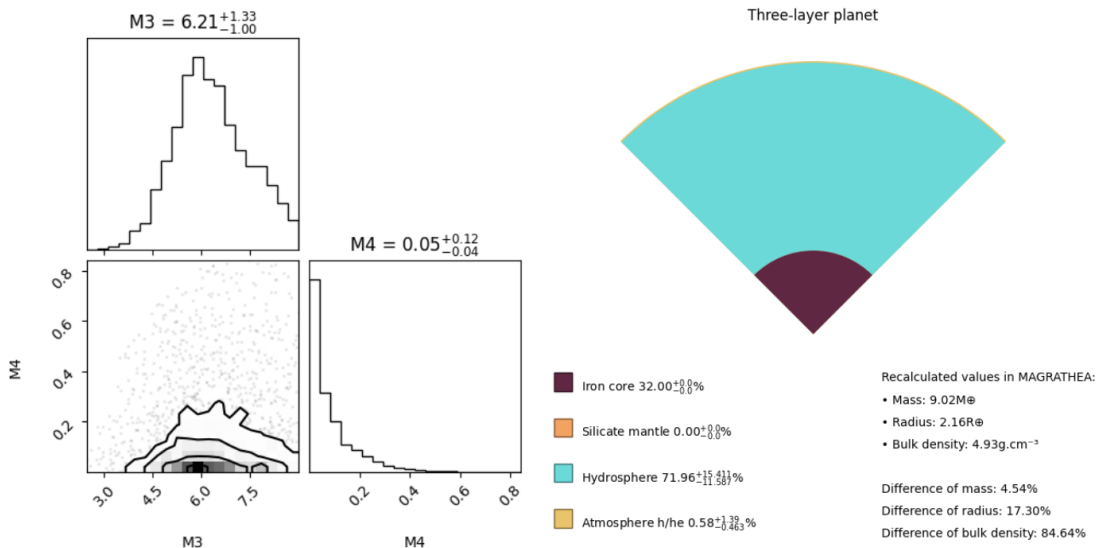


Figure 9: Output plots showing the results of the simulation. The first plot displays the corner plot results of a three-layer planet with a core, an hydrosphere, and an atmosphere with a mean molecular weight of 16.825 g.mol⁻¹. The second plot shows the mass distribution and the difference between the initial value and the simulation.

The impact of the mean molecular weight on the atmosphere and its dependency on the planet radius will be analyzed in Section 5.

5.0.3 Core

For this test, we are altering the core composition and investigating the effects of changing the equation of state (EOS) from a pure iron core to a mixture of iron and silicate. To achieve this, we are directly modifying the equation of state in the MAGRATHEA code. Initially, we are testing Fe-Si alloys with 7 weight percent Si, followed by 15 weight percent Si.

This test is aimed at favoring a formation pathway process. Indeed, pure iron cores can form in planets that differentiated early in their history, allowing iron, being a heavy element, to migrate towards the center due to the effect of gravity. On the other hand, mixed iron-silicate cores can form in planets where the

differentiation process has not been as efficient or where initial conditions favored a mixture of materials. Planets with mixed cores may present a more complex formation history and varied chemical interactions between core components. This difference in composition can manifest in the planet's magnetic field. A pure iron core can generate a strong planetary magnetic field due to the dynamo generated by the circulation of liquid iron. Conversely, a mixed iron-silicate core can have a weaker or more complex magnetic field, depending on the distribution of iron and silicates.

For this simulation we are fixing the mass of the core to see its impact on the hydrosphere and atmosphere, allowing us to compare the results with the previous study. We set the core mass to $2.7616M_{\oplus}$ and the mantle mass to 0. For the rest, we maintain the same assumptions as in Section 4.5 and run the model.

The left plot in Figure 10 shows the results for the Fe-Si alloys with 7 weight percent Si, and the right plot in Figure 10 shows the results for the Fe-Si alloys with 15 weight percent Si. The differences between the model and the results along with the loglikelihood value are given in Table 1.

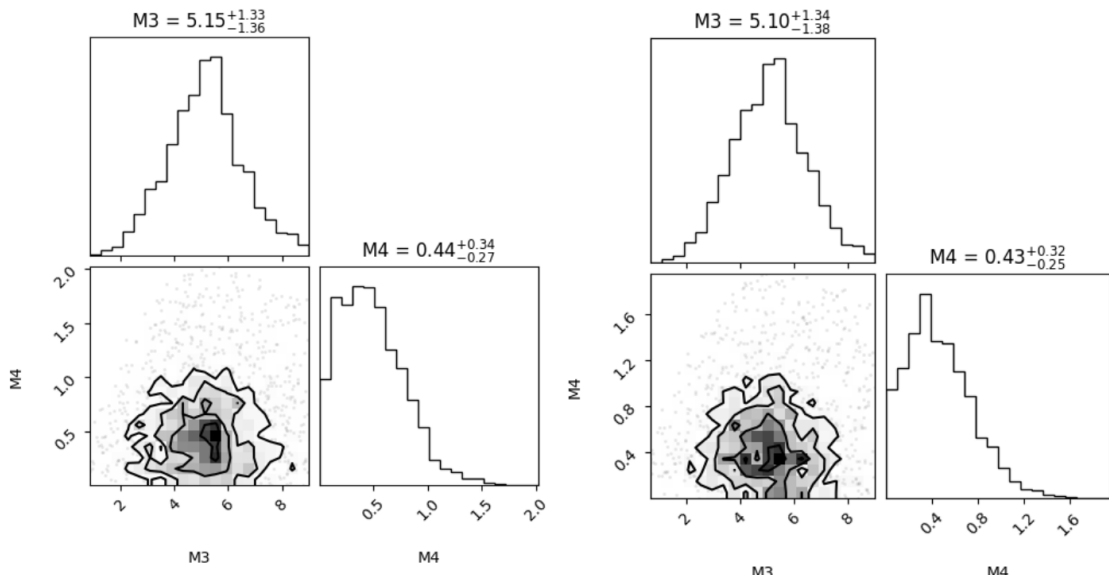


Figure 10: Corner plot results of a Fe-Si alloy core containing 7 weight percent Si on the left and 15 weight percent Si on the right.

5.1 Comparative analysis

Here, we focus on the study by Madhusudhan, Matthew C. Nixon et al. (2020) [29]. The authors simulated the interior composition of K2-18b using a model that includes a two-component Fe+rock core with an inner Fe layer and an outer silicate layer, a layer of H_2O , and an outer H/He envelope. This model bears similarities to MAGRATHEA, enabling us to test their three case scenarios for K2-18b with MAGRATHEA. The three cases are a rocky planet (Case 1), a gas-rich mini-Neptune (Case 2), and a Hycean world (Case 3). The composition ratios used in their study are based on those shown in Figure 3, where an Earth-like core is assumed to comprise 33% Fe, translating to 45% for Case 2, resulting in 14.85% Fe

and 30.15% Si. We aim to reproduce these cases using the same temperature and pressure assumptions we used previously to compare our results with theirs. The composition ratios for each case are summarized below:

- **Case 1 for K2-18b (Rocky Planet):** $M_{\text{tot}} = \{94.7\%, 0\%, 0.3\%, 5\%\}$
- **Case 2 for K2-18b (Gas-rich Mini-Neptune):** $M_{\text{tot}} = \{14.85\%, 30.15\%, 54.97\%, 0.03\%\}$
- **Case 3 for K2-18b (Hycean World):** $M_{\text{tot}} = \{3.3\%, 6.7\%, 89.994\%, 0.006\%\}$

The results from MAGRATHEA are summarized in the Table 1.

6 Discussion

In this section, the findings from the previous part will be summarized by highlighting the key observations and significant outcomes of the study, implications and considerations for K2-18b’s interior composition.

The key findings from all the simulations made in section 5 are summarized in the table below.

	In M_{\oplus}				In %			/
	M1	M2	M3	M4	diff_Mass	diff_Rad	diff_Dens	
Simulation 1	2.7616	0	$5.17^{+1.37}_{-1.39}$	$0.44^{+0.32}_{-0.25}$	2.99	11.41	39.39	-6.93 ± 0.145
Simulation 2	2.7616	$2.22^{+0.93}_{-0.76}$	0.1726	$0.33^{+0.13}_{-0.09}$	36.45	32.70	108.27	-25.67 ± 0.238
Simulation 3	2.7616	0	$6.21^{+1.33}_{-1.00}$	$0.05^{+0.12}_{-0.04}$	4.54	10.96	47.94	-15.84 ± 0.194
Simulation 4	2.7616	0	$5.15^{+1.33}_{-1.36}$	$0.44^{+0.34}_{-0.27}$	3.23	11.81	40.95	-6.75 ± 0.0923
Simulation 5	2.7616	0	$5.10^{+1.34}_{-1.38}$	$0.43^{+0.32}_{-0.25}$	3.92	11.86	40.18	-6.555 ± 0.2083
Case 1	8.17261	0	0.02589	0.4315	0	42.62	428.80	/
Case 2	1.281555	2.601945	4.743911	0.002589	0	12.04	46.77	/
Case 3	0.28479	0.57821	7.7664822	0.0005178	0	4.96	16.37	/

Table 1: Table of Different Models: Simulation are in the order they appeared in the previous section 4, along with the three paper’s Cases. Simulation 1: pure iron core with an hydrosphere and an atmosphere (with 3 g.mol^{-1}). Simulation 2: pure iron core with a mantle, an hydrosphere and an atmosphere (with 3 g.mol^{-1}). Simulation 3: pure iron core with an hydrosphere and an atmosphere (with $16.825 \text{ g.mol}^{-1}$). Simulation 4: Fe-Si alloys with 7 weight percent core with an hydrosphere and an atmosphere (with 3 g.mol^{-1}). Simulation 5: Fe-Si alloys with 15 weight percent core with an hydrosphere and an atmosphere (with 3 g.mol^{-1}).

The model that most accurately reflects the observed data is the Hycean world model (Case 3). It shows the lowest variance in key parameters - mass, radius, and density - making it the most coherent with the observed data. Moreover, Case 1 and Simulation 2, both sharing a high content of rocky material, exhibit significant discrepancies in density, suggesting again that K2-18b likely consists of low-density materials to match its observed density. If K2-18b indeed hosts a substantial amount of water as favored by the model, it would potentially inaugurate a new classification of planets.

As previously mentioned, for the five Simulations using our model, the three-layer planet is favored (highest log-likelihood value) and initial difference calculation. However, in reality, we do not know which configuration is more probable, and a three-layer planet with a core, mantle, and atmosphere could also have been possible. This scenario never converged, so it was not included in this report, but it remains a plausible interior composition for K2-18b, with the possibility of an atmosphere that could be vastly extended to match the observed density.

When the mean molecular weight increases, it results in a significantly less extended atmosphere of $0.05M_{\oplus}$ compared to the original H/He mix, which gives an atmosphere of $0.44M_{\oplus}$. This change implies that atmospheres with a lower mean molecular weight have lower total atmospheric mass. Even more interestingly, the simulations show less difference between the observed values and the simulated values for the low mean molecular weight atmosphere. This outcome should not be possible when considering the observed transmission spectra. This discrepancy suggests that the actual atmosphere may be deeper as it would require a smaller amount of heavy molecules to achieve the same accuracy or that the heavy molecules might be confined to specific layers or regions of the atmosphere, rather than being uniformly mixed throughout. The findings highlight the need for adjustments in the atmospheric models used, see section 7.

For the core Fe-Si alloys simulations, the difference in results is very small. The simulation that seems to better replicate the density and distribution of materials in the core, when looking at the other layers, is the 15 weight percent Si model with a lower log-likelihood value. This also aligns with Case 3, which includes a constrained iron and silicate layer. The presence of more silicate might stabilize certain phases or structures within the core, leading to a more accurate representation of the planet’s interior. This suggests that the formation of the building blocks of K2-18b could have occurred late in the history of its protoplanetary disk. This is particularly intriguing, as we currently do not fully understand how planets sub-Neptune like K2-18b formed.

7 Perspectives

In this section, we will analyze potential future work that can enhance our model.

- Atmosphere:

To enhance the study of K2-18b’s interior composition and refine our model, our primary focus should be on understanding its atmosphere. For instance we could calculate and incorporate the temperature gradient of the planet’s atmosphere. Such study have been proposed for K2-18b with Exo-REM, a 1D radiative-equilibrium model[57]. Additionally, using cloud-resolving simulations of the planetary atmosphere[58] could provide further insights and refinement to the cloud mapping and potential water cycle. Ultimately, a deep atmosphere presents different challenges and considerations compared to a shallow one. Achieving a deeper understanding requires advancements in instrumentation to probe deeper into the atmosphere.

- Host star:

In addition, considering stellar activity in our model is essential as it profoundly influences the presence and chemical composition of an atmosphere. For instance, a small planet subjected to excessive irradiation might either lose its atmosphere entirely or develop unique gas signatures due to potential surface magma as discussed in section 2.4. Examining the atomic composition of planetary atmospheres and comparing them to their host stars' atoms could also enhance our understanding. Through the study of numerous stars, we can uncover potential correlations by employing machine learning tools to predict the atmospheric composition of a planet based on its host star's characteristics.

- Magnetism:

To better understand the planet's core, we could analyze its magnetic field. Planets with strong magnetic fields can deflect their host star wind, create radiation belts, or exhibit charged particles in their atmospheres. Another approach is studying radio emissions from the planet, which can be influenced by its magnetic field.

- Other planets:

Understanding the interior composition of planets within our own solar system is crucial. Additionally, studying the interiors of nearby planets, such as those in the TRAPPIST-1 system, could also provide valuable insights¹⁹.

8 Limitations

It is important to acknowledge the inherent limitations of the models discussed here. Beyond the general problem of degeneracy, one significant issue is the assumption of distinct layers (e.g., mantle, hydrosphere, atmosphere) without considering potential mixing, such as between rock and water layers, or transitional zones between these layers. In some planetary scenarios, ice and rock layers may remain mixed for billions of years unless significant mass loss processes occur. Planetary interiors in reality exhibit fluid dynamics, chemical interactions, and phase changes that are not fully captured by these models.

Furthermore, the equations used in MAGRATHEA are based on terrestrial data and may not fully apply to diverse exoplanetary environments. Uncertainties in input parameters such as planetary mass, radius, and atmospheric composition can propagate into the model predictions and result in large final uncertainties.

Additionally, some combinations we attempted with the model were deemed impossible or too complex by MAGRATHEA. However, the limitations of the model do not necessarily mean that these configurations could not exist in reality. This underscores the need for continued refinement and exploration of planetary interior modeling to better understand the full range of possible planetary compositions and structures.

¹⁹Source: https://www.researchgate.net/publication/331259714_Geophysical_assessment_of_habitability_for_the_TRAPPIST-1_exoplanets

9 Conclusion

This project aimed to develop a model for the interior of small exoplanets using MAGRATHEA combined with UltraNest, despite the challenge of degenerate composition. This issue is particularly significant due to the growing number of exoplanet discoveries and atmospheric characterization. Additionally, this research sought to understand the diversity of planetary compositions beyond our solar system, unraveling the potential for their habitability.

This model has been applied to the exoplanet K2-18b to better understand its nature. Different compositions for its interior were studied, with an analysis of its atmosphere and the impact of core changes, along with comparisons to another study. The results revealed a preference for a Hycean world, with an extended atmosphere and a core made of an iron-silicate mix.

These findings on the modeling of sub-Neptune planets can be confirmed or refuted by future observations from the JWST and upcoming missions such as ARIEL from ESA in 2029. Although K2-18b will be too cold for the range of this spacecraft, this mission will aim to constrain the chemistry of many exoplanets. It will link their atmospheric composition to the chemistry of their host star, providing new key insights to unravel their interior composition.

References

- [1] Natalie M. Batalha, Jason F. Rowe, and Stephen T. Bryson. 2013. *ApJS*, 204, 24.
- [2] Chenliang Huang, David R. Rice, and Jason H. Steffen. 2022. *MNRAS*, 513, 4, 5256–5269.
- [3] Todd J. Henry et al. 2006. *AJ*, 132, 2360z.
- [4] C. Reylé and K. Jardine et al. 2021. *AA*, 650, A201.
- [5] A. S. Brun, J. Bouvier, and P. Petit et al. 2023. *AA*, 650, A201.
- [6] S. Seager and G. Mallén-Ornelas. 2003. *AJ*, 585, 1038–1050.
- [7] C. Cadieux, M. Plotnykov, R. Doyon, and et al. 2024. *ApJL*, 960, L3.
- [8] Frederick Adams and Gregory Laughlin. 2004. *Revista Mexicana de Astronomía y Astrofísica*, 36, 3–12.
- [9] Rory Barnes. 2017. *Celestial Mechanics and Dynamical Astronomy*, 129, 509–536.
- [10] James R. A. Davenport. 2016. *ApJ*, 829, 23.
- [11] Elisabeth R. Newton, Jonathan Irwin, and David Charbonneau et al. 2016. *ApJL*, 821, L19.
- [12] Antígona Segura. 2018. Springer, Cham, 2995–3017.
- [13] Brice-Olivier Demory et al. 2017 Michaël Gillon, Amaury H. M. J. Triaud. *Nature*, 542, 456–460.
- [14] John Barnes-et al. 2016 Guillem Anglada-Escudé, Pedro J. Amado. *Nature*, 536, 437–440.
- [15] David W. Hogg et al. 2015 Daniel Foreman-Mackey, Benjamin T. Montet. *ApJ*, 806, 215.
- [16] Christophe Lovis and Debra A Fischer. 2010. Radial Velocity.
- [17] Ji Wang, Debra A. Fischer, and Elliott P. Horch et al. 2014. *ApJ* 799 229.
- [18] Thaddeus D. Komacek. 2021 Jonathan J. Fortney, Rebekah I. Dawson. *AGU*, 126, 3.
- [19] Jacob L. Bean, Sean N. Raymond, and James E. Owen. 2021. *Journal of Geophysical Research: Planets*, 126, 1.
- [20] Hannah Diamond-Lowe, Laura Kreidberg, and C E Harman et al. 2022. *AJ* 164 172.
- [21] J. E. Owen, I. F. Shaikhislamov, and H. Lammer et al. 2020. *Space Science Reviews*, 216, 11, 1-24.
- [22] Benjamin J. Fulton, Erik A. Petigura, and Andrew W. Howard et al. 2017. *American Astronomical Society*, 154, 109.
- [23] Nikku Madhusudhan, Anjali A A Piette, and Savvas Constantinou. 2021. *ApJ*, 918, 1.
- [24] Björn Benneke, Michael Werner, and Erik Petigura et al. 2017. *ApJ*, 834, 187.
- [25] Leonardo A. dos Santos, David Ehrenreich, and Vincent Bourrier et al. 2020. *AA*, 634, L4.
- [26] Björn Benneke, Ian Wong, and Caroline Piaulet et al. 2019. *ApJL*, 887, L14.
- [27] R. Cloutier, N. Astudillo-Defru, and R. Doyon et al. 2017. *AA*, 608, A35.
- [28] Nikku Madhusudhan, Subhajit Sarkar, and Savvas Constantinou et al. 2023. *ApJL*, 956, L13.
- [29] Nikku Madhusudhan, Matthew C Nixon, and Luis Welbanks et al. 2020. *ApJL*, 891, L7.
- [30] Renyu Hu, Mario Damiano, and Markus Scheucher et al. 2021. *ApJL*, 921, L8.
- [31] Shang-Min Tsai, Hamish Innes, and Tim Lichtenberg et al. 2021. *ApJL*, 922, L27.
- [32] Xinting Yu, , and Julianne I. Moses et al. 2021. *ApJ*, 914, 38.
- [33] Sean N. Raymond, Andre Izidoro, and Alessandro Morbidelli. 2018. *Planetary Astrobiology*, 12.
- [34] Vardan Adibekyan, Caroline Dorn, and Sérgio G Sousa et al. 2021. *374*, 6565, 330-332.
- [35] John W Morgan, Edward ANDERSt, and MnS Cu et al. 1980. *Proceedings of the National Academy of Sciences*, 77, 12.

- [36] Katharina Lodders. 2003. *ApJ*, 591, 1220.
- [37] Keith D. Putirka, Caroline Dorn, and Natalie R. Hinkel et al. 2021. *17*, 4, 235-240.
- [38] Haiyang S. Wang, Charles H. Lineweaver, and Trevor R. Ireland. 2018. *Icarus*, 299, 460-474.
- [39] Haiyang S. Wang, Charles H. Lineweaver, and Trevor R. Ireland. 2018. *Icarus*, 328, 287-305.
- [40] Joshua. 2010 N. Winn. University of Arizona Press, 55-77.
- [41] John Southworth. 2011. *MNRAS*, 417, 3, 2166–2196.
- [42] Oliver Shorttle, Sean Jordan, and Harrison Nicholls et al. 2024. *ApJL*, 962, L8.
- [43] Raymond F. Smith, Dayne E. Fratanduono, and David G. Braun et al. 2018. *Nature Astronomy*, 2, 452–458.
- [44] June K. Wicks, Raymond F. Smith, and Dayne E. Fratanduono et al. 2018. *Science Advances*, 4, 4.
- [45] Kei Hirose, Stéphane Labrosse, and John Hernlund. 2013. *Annual Review of Earth and Planetary Sciences*, 41, 657-691.
- [46] Oliver Tschauner, Ma Chi, and John R. Beckett et al. 2014. *Science*, 346, 6213, 1100-1102.
- [47] Aaron S. Wolf and Dan J. Bower. 2018. *Physics of the Earth and Planetary Interiors*, 278, 59-74.
- [48] Artem R. Oganov and Shigeaki Ono. 2004. *Nature*, 430, 445–448.
- [49] Takeshi Sakai, Haruhiko Dekura, and Naohisa Hirao. 2016. *Scientific Reports*, 6, 22652, 1-8.
- [50] Diana Valencia, Dimitar D. Sasselov, and Richard J. O’Connell. 2007. *ApJ*, 656, 545.
- [51] A. N. Dunaeva, D. V. Antsyshkin, and O. L. Kuskov. 2010. Springer, 44, 202–222.
- [52] Rainer Feistel and Wolfgang Wagner. 2006. *J. Phys. Chem.*, 35, 1021–1047.
- [53] Lorena Acuna, Magali Deleuil, and Olivier Mousis et al. 2021. *AA*, 647, A53.
- [54] Lucile Bezacier, Baptiste Journaux, and Jean Philippe Perrillat et al. 2014. *J. Chem. Phys.* 141, 104505.
- [55] Zachary M. Grande, C. Huy Pham, and Dean Smith et al. 2022. *American Physical Society*, 105, 10.
- [56] Paula Sarkis, Thomas Henning, and Martin Kürster et al. 2018. *AJ*, 155, 257.
- [57] B. Charnay D. Blain and B. Bézard. 2021. *AA*, 646, A15.
- [58] Noé Clément et al. 2024 Jérémie Leconte, Aymeric Spiga. *AA*, 686, A131.